UCL/HEP 00

Signatures of Multiparton Interactions in Three-Jet Photoproduction Events at HERA

1st Year Transfer Report

C.Gwenlan
University College London

Abstract

A study of the angular distributions of events containing at least three, high transverse energy jets is presented. Monte Carlo models indicate little sensitivity to multiple parton scattering at high invariant masses of the three-jet system. However, at low invariant masses, a strong sensitivity is observed. In particular, the distribution of the variable, ψ_3, which reflects the orientation of the lowest energy jet, tends towards a uniform population of phase space in models where multiparton interactions have been included. This effect is significant enough to be measured with the ZEUS detector. A preliminary comparison with the data suggests that, at low three-jet invariant masses, the distributions may be described significantly better by models in which a simulation of multiple scattering has been included.

Submitted in fulfillment of the requirements for transfer
from M.Phil to Ph.D. status.

Contents

List of Figures

List of Tables

1 Introduction

Since 1992, the ZEUS detector has been used to study the photoproduction of jets resulting from electron-proton (ep) collisions taking place in the HERA accelerator. Events are classified as photoproduction processes when a quasi-real photon is exchanged between the electron and proton. At leading order (LO) in QCD, two components of the cross-section have been identified [1]. These components are termed *direct* and *resolved*. In direct photoproduction, the photon couples directly to a parton in the proton and contributes all of its energy to the hard scatter. However, in the resolved case the photon acts as an extended source of partons, one of which scatters from a parton in the proton, and contributes only a fraction of the total photon momentum. Beyond LO in QCD, this simple distinction between direct and resolved events is no longer precisely defined.

In resolved photoproduction events, it is possible for more than one hard scatter to occur in a single γp collision. These *multiple scattering events* are expected to have consequences which should be observable in the final hadronic state. In extreme cases, the transverse energy of the secondary scatters may be enough to produce further jets. Consequently, the effects of multiparton interactions may be particularly important in final states containing more than two jets.

The angular distributions of events containing three or more high transverse energy jets, with a three-jet invariant mass of greater than 50GeV, has been the subject of a previous study carried out by the ZEUS Collaboration [2]. In this kinematic regime, the angular distributions are well described by parton shower models and $\mathcal{O}(\alpha\alpha_s^2)$ perturbative QCD calculations, but are inconsistent with a uniform population of phase space. In addition, the models are found to be insensitive to multiparton interactions. Consequently, it has been deduced that, in this energy regime, the third jet arises from parton showering and is not due to a second hard scatter. A more detailed overview of these results is given in Appendix A.

In this report, we present a study of the three-jet angular distributions in four separate kinematic regimes. These regimes have been selected by placing different constraints on the invariant mass of the three-jet system, whilst keeping the conditions imposed on the transverse energies of the jets the same. As found by the ZEUS Collaboration, we expect the model distributions to show little or no sensitivity to multiparton interactions in the higher energy regions. However, at lower energies, the effects of multiple parton scattering may be significant. Any secondary interactions are entirely independent of the primary hard scatter and so the orientation of a third jet arising from a second scatter should not depend upon the distribution of the primary jets. In QCD, the azimuthal (around the beam-line) orientations of jets are randomly distributed throughout phase space. Therefore, we would expect that if multiparton interactions form a significant contribution, the distribution of a variable which reflects the azimuthal orientation of the lowest energy jet, with respect to the primary jets, should tend towards a uniform population of the available phase space. In the work that follows, we present a set of Monte Carlo results and compare the distributions for models both with and without a simulation of multiple parton scattering. In addition, we give a preliminary comparison with a sample of ZEUS data obtained during the 1997 running period. The data collected correspond to an integrated luminosity of $\sim 26\text{pb}^{-1}$.

2 Kinematics of Lepton-Proton Scattering

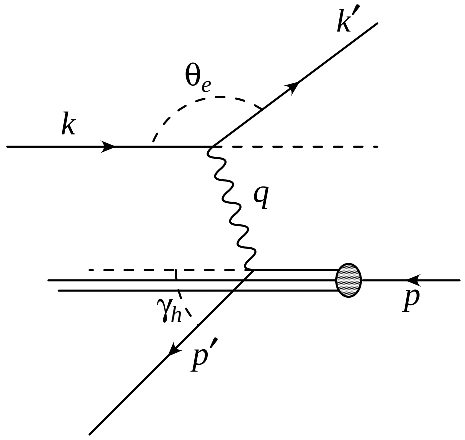

Figure 1: *Kinematics of lepton-proton scattering*

Lepton-proton scattering may occur via the electromagnetic or the weak interaction. When the exchanged boson is a photon or a Z°, the process is said to be a Neutral Current (NC) event. Conversely, when the interaction is mediated by a $W^{\pm}$, the process is classified as Charged Current (CC). In this section we consider the kinematics of lepton-proton scattering in the case where the exchanged boson is a photon.

In Figure 1, the 4-momenta of the incoming and scattered lepton are $k = (E, \mathbf{k})$ and $k' = (E', \mathbf{k}')$ and the 4-momenta of the proton and photon are $p = (E_p, \mathbf{p})$ and $q = (E_\gamma, \mathbf{q})$. For a given centre of mass energy $\sqrt{s} = \sqrt{(k+p)^2}$, it is possible to completely describe the kinematics of lepton-proton scattering using any two of the three Lorentz invariant quantities,

$$Q^2 = -q^2 = -(k - k')^2 \tag{1}$$

$$y = \frac{q.p}{k.p} \tag{2}$$

$$x = \frac{-q^2}{2p.q} \tag{3}$$

where the 4-momentum transfer, q, between the lepton and the proton system is given by $q = k - k'$. The quantity Q^2 is the negative square of the momentum of the exchanged boson, and is often referred to as its *virtuality*.

In the proton rest frame, $y \approx \frac{E_\gamma}{E_e}$ and so is interpreted as the fraction of the electron beam energy carried by the photon in the proton rest frame. In the infinite momentum frame, where the probe has arbitrarily large momentum, x corresponds to the fraction of the proton's momentum taking part in the interaction.

The above three quantities are related to each other and the centre of mass energy squared, via the simple relation,

$$Q^2 = s.x.y \tag{4}$$

where we have taken the energy to be high and so have neglected all masses.

In the case of photon exchange, the propagator is given by $\frac{-ig_{\mu\nu}}{q^2}$. Therefore, the cross-section falls as $\sim \frac{1}{Q^4}$, causing the low Q^2 processes to dominate.

In lepton-proton collisions, where Q^2 is large, it is this variable itself that provides the hard scale for perturbative calculations. Perturbative calculations can be applied down to a scale of $Q^2 \approx \Lambda^2_{QCD}$. Experimentally, Λ_{QCD} has a value of approximately 0.2 ± 0.1GeV [3]. Events where Q^2 is large compared to Λ^2_{QCD} are called *Deep Inelastic Scattering* (DIS) events.

For low Q^2, events are dominated by the exchange of quasi-real photons with virtuality $Q^2 \approx 0$. Such events are called *photoproduction* processes. The lifetime of the exchanged photon varies approximately as $\sim \frac{E_\gamma}{Q^2}$. Thus, for very low virtualities, the lifetime of the photon is long compared to the characteristic time of the hard subprocess. This means that the electron beam can be considered as a source of approximately massless, collinear photons. When Q^2 is very small it can no longer be viewed as the hard scale in the interaction. In order to allow the possibility of comparing experimental results with perturbative QCD calculations, we require some alternative hard scale. This is usually taken to be the transverse energy of the observed jets, E_T^{jet}.

3 Photoproduction

In this work, we have studied the low Q^2 photoproduction events, mentioned above. Below, we describe the two types of photoproduction event (direct and resolved). For simplicity in this discussion, we concentrate particularly on the LO processes, which produce two jets in the final state. Beyond LO, hard photoproduction involves processes which produce final states containing three or more jets.

3.1 Direct Photoproduction

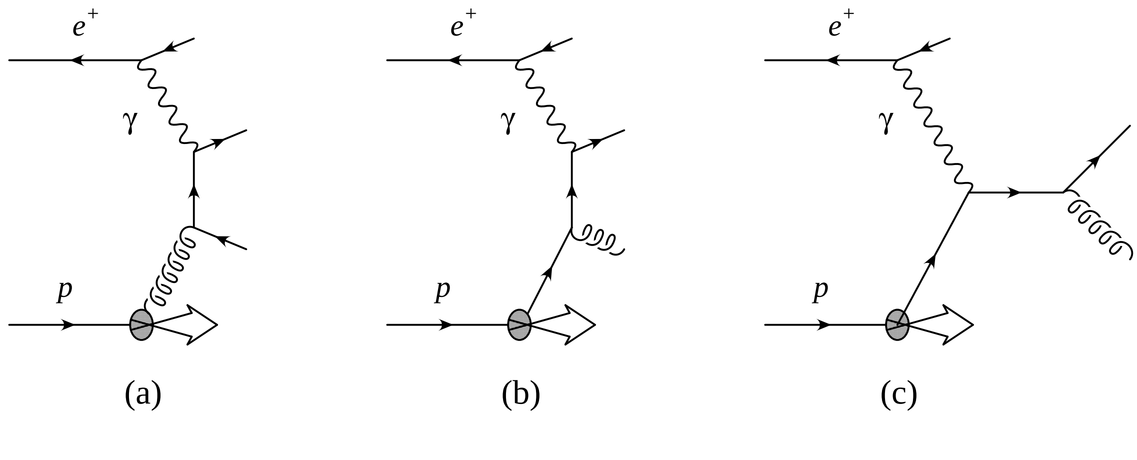

Figure 2: *Lowest order direct photoproduction processes*

In direct photoproduction, the photon interacts as a point-like particle via the electromagnetic interaction. Since the photon contributes all of its energy to the hard subprocess, the final state is expected to have a higher transverse momentum than resolved photon events, where only a fraction of the photon's momentum participates.

Figure 2 shows the three possible LO direct photoproduction diagrams. In Figure 2(a) the photon couples to a quark arising from a "split" gluon in the proton which produces a quark anti-quark pair. This is termed boson-gluon fusion. Figures 2(b) and 2(c) both show the QCD Compton process. In this process a photon couples to a quark within the proton which then radiates a gluon before hadronisation. In Figure 2(b), the quark from the proton emits Initial State Radiation (ISR) before coupling to the photon. In each of the diagrams above, the final state consists of two jets, a scattered electron and a proton remnant.

3.2 Resolved Photoproduction

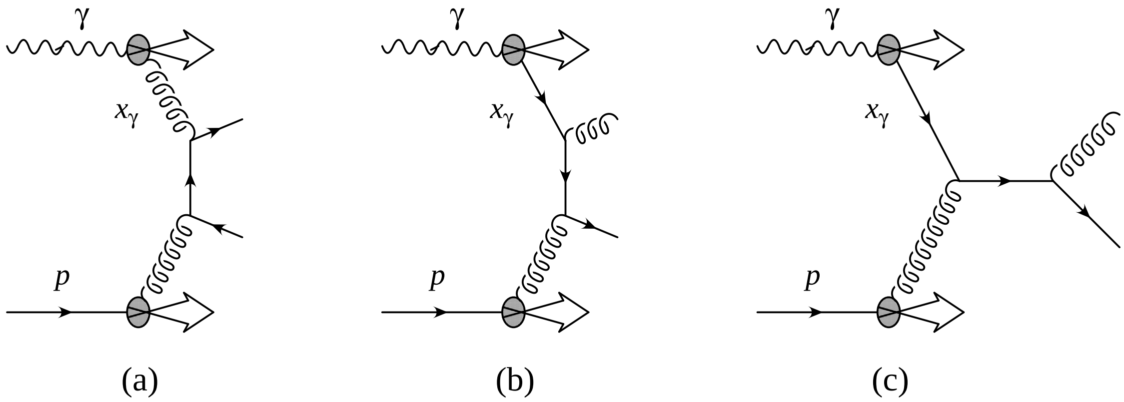

Figure 3: *Lowest order resolved photoproduction processes*

In a resolved photoproduction event, the photon acts as a source of partons and interactions take place between partons in the hadronic photon and those in the proton. In such events, the photon contributes only a fraction, x_γ, of the total photon energy to the hard subprocess. Fluctuations of photons into $l\bar{l}$ states are well understood within the framework of electroweak interactions. However, fluctuations into $q\bar{q}$ states are much more complicated. Resolved photoproduction events arise because, at low Q^2, the lifetime of the photon is long enough for fluctuations to low virtuality $q\bar{q}$ states to develop a complex hadronic structure, which cannot be described by perturbative methods alone.

There are many diagrams for LO resolved processes, three of which are shown in Figure 3. In Figure 3(a), a gluon from the photon interacts with a gluon from the proton. This process is termed gluon-gluon fusion. In Figure 3(b) and 3(c) a quark from the photon interacts with a gluon from the proton. In each case, the final state consists of two jets, a scattered electron, a proton remnant and a photon remnant.

3.3 Multiparton Interactions

In resolved photoproduction processes, the photon interacts as an extended object and there is a significant probability for greater than one interaction between partons from the colliding proton and the hadronic photon. Any secondary scatters are independent of the primary hard interaction. A schematic representation of a multiple scattering event is shown in Figure 4. The probability of multiparton interactions occurring increases at low x_γ, where the parton density is high [4], since a larger fraction of the photon remnant is available for secondary interactions. By definition, secondary interactions have a lower transverse momentum than the primary hard scatter, which means that the final state will consist of the hard interaction and zero or more softer interactions. However, in extreme cases, the transverse energy of the secondary scatters may be enough to produce further jets.

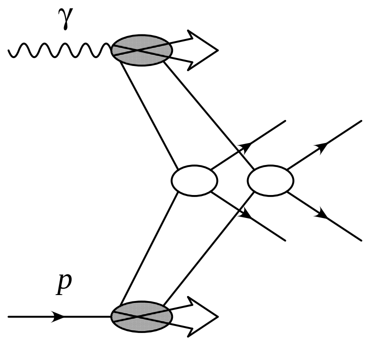

Figure 4: *Multiparton interactions in a single photon-proton collusion*

Events with direct photons cannot contain multiparton interactions. Therefore, photoproduction at HERA offers the unique opportunity to compare events both with and without the possibility of multiple scattering in the same physical environment. This allows studies to be made on the effects of these additional interactions. Such studies are important, not only for increasing our understanding of the physics being carried out at HERA, but also for the physics taking place at both current and future hadron colliders such as the Tevatron and the Large Hadron Collider (LHC). In this report we search specifically for signatures of multiparton interactions in three-jet events, in an attempt to observe their effects in a relatively unambiguous experimental and theoretical regime.

4 The ZEUS Detector

A detailed description of ZEUS and its component detectors may be found in references [5, 6]. The main components important for the present analysis are the Central Tracking Detector (CTD) and the Uranium-scintillator sampling CALorimeter (UCAL). In this section, we give a brief description of these components.

4.1 The Central Tracking Detector

The Central Tracking Detector (CTD) is a drift chamber, consisting of 72 cylindrical layers, which are arranged in 9 superlayers. The CTD covers the polar angle[1] region $15^\circ < \theta < 164^\circ$ and is contained within a superconducting solenoid, which produces a field of 1.43T. In the present work, the CTD was used to establish an interaction vertex for each event. Information from the CTD was also used in the trigger selection.

4.2 The Uranium Calorimeter

Outside the superconducting solenoid lies the ZEUS CALorimeter (CAL). This consists of the high resolution UCAL and a BAcking Calorimeter (BAC). The main calorimetry is performed by the UCAL which is divided into three sections; the Forward (FCAL), Rear (RCAL) and Barrel (BCAL) CALorimeters. The coverage of the UCAL in pseudorapidity[2] is $4.3 \geq \eta \geq -3.8$. The UCAL is hermetic and consists of 5918 cells, each read out by two photomultiplier tubes. The energy resolution of the UCAL, as measured under test beam conditions, is $\frac{18\%}{\sqrt{E}} \oplus 1\%$ for electrons and $\frac{35\%}{\sqrt{E}} \oplus 2\%$ for hadrons (where E is in GeV). For the present work, the energy deposits in the UCAL were used in the jet-finding and in measuring the jet energies. Information from the CAL was also used in the trigger selection.

5 Event Reconstruction and Jet Algorithms

In this section, we state the ways in which the kinematic variables important for photoproduction are reconstructed. In addition, we give a brief description of the jet algorithm used throughout this work. A more detailed description of the reconstruction of kinematic variables and of the jet algorithms used within the ZEUS Collaboration are given in Appendices B and C, respectively.

5.1 Reconstruction of Kinematic Variables

The kinematic variables important for photoproduction are not directly measurable. Therefore, they must be reconstructed from quantities that can be determined experimentally. In this section, we state the equations used to reconstruct the variables, y and Q^2, via both the "electron method" and the "Jaquet-Blondel method" [7]. In addition, we define the equations relevant for the reconstruction of the variables x_p and x_γ.

[1]The ZEUS detector uses a right-handed, orthogonal coordinate system, with the z-axis being defined to be in the direction of the proton and the x-direction pointing towards the centre of the HERA ring. Polar angles, θ, are measured with respect to the z-axis.

[2]Pseudorapidity is defined as $\eta = -\ln(\tan \frac{\theta}{2})$.

5.1.1 Reconstruction of y and Q^2

If the scattered lepton is observed in the detector, the variables y and Q^2 can be obtained from the equations,

$$y_e = 1 - \frac{E'_e}{2E_e}(1 - cos\theta_e) \tag{5}$$

$$Q^2_e = 2E_eE'_e(1 + cos\theta_e) \tag{6}$$

where E_e and E'_e are the incoming and outgoing lepton energies, respectively, and θ_e is the scattered lepton angle with respect to the proton beam direction. At low Q^2, θ_e will be large. Therefore, the experimental definition of photoproduction in ZEUS is the absence of the scattered lepton in the UCAL. This corresponds to scattering angles of greater than $\sim 177^o$ and $Q^2 \lesssim 1\mathrm{GeV}^2$.

The variables y and Q^2 may also be reconstructed from hadronic energy deposits in the calorimeter, via the Jacquet-Blondel expressions,

$$y_{JB} = \frac{\sum_i(E_i - p_{zi})}{2E_e} \tag{7}$$

$$Q^2_{JB} = \frac{(\sum_i p_{xi})^2 + (\sum_i p_{yi})^2}{1 - y_{JB}} \tag{8}$$

In the above expressions, the sums run over all cells of the UCAL except for those where the scattered lepton enters the detector.

5.1.2 Reconstruction of x_p and x_γ

In order to reconstruct the variables x_p and x_γ the following operational definitions are used, where the sum runs over only the two jets of highest transverse energy,

$$x_p^{OBS} = \frac{\sum_{jets1,2} E_T^{jet} \exp{(\eta^{jet})}}{2E_p} \tag{9}$$

$$x_\gamma^{OBS} = \frac{\sum_{jets1,2} E_T^{jet} \exp{(-\eta^{jet})}}{2yE_e} \tag{10}$$

Provided that all events are treated consistently in both theory and experiment, the above definitions of x_p^{OBS} and x_γ^{OBS} are defined to all orders of perturbation theory.

5.2 Jet-Finding

Two types of jet algorithm are used within the ZEUS Collaboration; namely, the cone and clustering algorithms. In the work presented in this report, the jet-finder used is the KTCLUS [8, 9] algorithm in the inclusive mode [10]. This is a clustering algorithm which combines objects with small relative transverse energy into jets. It is invariant under Lorentz boosts along the beam axis and is ideal for the study of multijet events since, unlike cone algorithms such as EUCELL [11] and PUCELL [12], it suffers from no ambiguities due to overlapping jets.

6 Data Selection

During the 1997 running period, HERA collided protons at 820GeV with positrons at 27.52GeV. In this section, we give an overview of the process of data selection relevant to the current work. We begin by giving a brief description of the ORANGE package, which was used to obtain the data. Following this, we describe the method by which a suitable set of clean photoproduction data was selected.

6.1 ORANGE

The Overlying Routine for Analysis Ntuple GEneration (ORANGE) is part of a recent move to expand and update the existing physics analysis environment used at the ZEUS experiment. ORANGE is a flexible, general purpose top layer of code to the analysis environment. This code calls all the major ZEUS software packages and stores over 250 variables in an ntuple. Currently, ORANGE is still in the developmental stage, although the first version is due for imminent release. It is intended that this top layer will eventually become an integral part of almost all analyses performed in the ZEUS Collaboration. The ORANGE top layer will be responsible for $\sim$ 90% of the common calls used in an analysis whilst the user is free to develop the remaining 10% of code, according to their specific requirements.

6.2 Triggers

ZEUS uses a three-level trigger [6] to select data online. The First Level Trigger (FLT) is a hardware trigger. At the FLT, only a limited amount of information about event properties is available. The criteria that must be satisfied at the FLT are based primarily on global or regional energy sums in the calorimeter, together with simple tracking requirements from the CTD FLT and vetoes from additional components. The Second Level Trigger (SLT) is a software trigger. At the SLT, more time is available and triggers can be used with more sophisticated algorithms and more complete detector information than is available at the FLT. The SLT has selection criteria based on simple tracking requirements and calorimeter energy sums which ensure that high transverse energy events are accepted. The Third Level Trigger (TLT) is a software trigger running on a farm of very fast processors. At the TLT, more time is available and more complete detector information can be obtained. After the TLT selection, events go through a complete offline reconstruction and pass through additional offline filters. For the work presented here, the HPP dijet filter was used, which makes decisions based on calorimeter quantities and the finding of dijet events. In order to identify jets, the TLT uses a simplified version of the EUCELL jet-finder (EUTLT) which runs over the cells in the calorimeter.

6.3 Offline Cleaning Cuts

Following the trigger selection, the data still suffers some contamination from beam-gas and cosmic ray backgrounds as well as from NC and CC DIS events. Therefore,

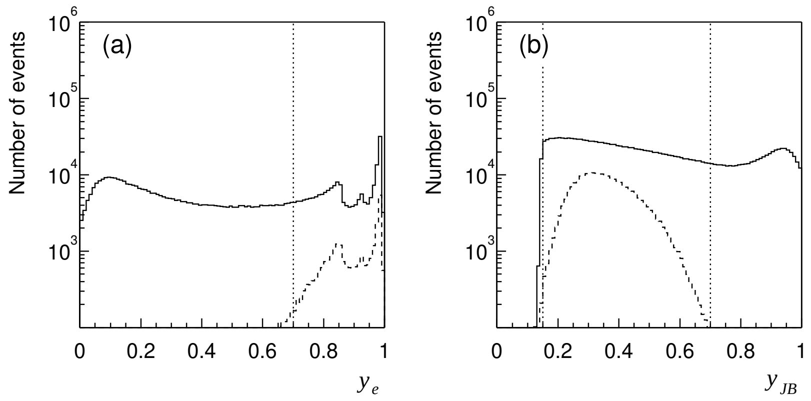

Figure 5: (a) y_e *and* (b) y_{JB} *distributions for: the DST selected sample of events (solid histogram) and the LUMI tagged sample of events (dashed histogram). The vertical dotted lines indicate the cuts that have been imposed. The vertical lines indicate the cuts that have been imposed*

additional offline cleaning cuts are applied. A suitable set of cleaning cuts was determined by comparing the DST (trigger) selected sample of events with those of a LUMI tagged sample. An event is said to be LUMI tagged if an electron or positron has been identified in the LUMI_e detector[3], with energy $5\mathrm{GeV} < E_e^{LUMI} < 20\mathrm{GeV}$ and if there is little or no corresponding energy in the LUMI_γ detector such that $E_\gamma^{LUMI} < 2\mathrm{GeV}$. It can be assumed that the LUMI tagged sample of events is essentially free of background. The distributions that were compared involved quantities that were constructed using both tracking and calorimeter information.

In order to reject residual beam-gas and events due to cosmic ray background, cuts using the final z-vertex position, other tracking information and calorimeter timing information were applied. CC DIS events were removed by placing a cut on the missing transverse energy, as measured by the CAL. NC DIS events, with an identified positron candidate in the CAL, were removed from the sample by requiring NO positron satisfying the requirements that $y_e < 0.7$ and $E_e > 5\mathrm{GeV}$. A positron is said to have been found if the electron-finder SINISTRA [13] gives a probability of greater than 0.9 that a candidate has been identified. The cut on y_e does not remove DIS events where the positron was correctly identified to have $y_e < 0.7$. Neither does it remove events where the positron entered the detector but was not identified. For any remaining NC DIS events, for which the scattered positron entered the UCAL, the value of y_{JB} will be close to unity. Therefore, the requirement that $y_{JB} < 0.7$ was made. A lower cut of $y_{JB} > 0.15$ was also imposed, which rejects beam-gas events. The distributions of y_e and y_{JB} are shown in Figure 5. The vertical dotted lines indicate the cuts that were imposed.

The cuts described in this section restrict photon virtualities to be less than $\sim 1\mathrm{GeV}^2$ with a mean of $\sim 10^{-3}\mathrm{GeV}^2$.

[3]The LUMI detector consists of two lead scintillators located at $z = -34\mathrm{m}$ and $z = -104\mathrm{m}$ in the direction of the electron beam. These provide ZEUS with luminosity measurements and tagged photoproduction events.

7 Monte Carlo Event Simulation

In order to produce the work presented in this report, events from the HERWIG 5.9 [14] and PYTHIA 6.140 [15] event generators have been used. The reason for using more than one generator is so that an estimate of the model dependence of the parameters being generated or the cross-section being extracted may be determined. A description of the details of implementation of the HERWIG and PYTHIA programs, including an overview of their treatment of multiparton interactions, can be found in Appendix D.

In both Monte Carlo programs, direct and resolved events were generated separately. The samples of direct and resolved photoproduction were then combined to form a single set of hard photoproduction events. The combination was carried out according to the ratio of the total cross-section for each process, as calculated by the respective Monte Carlo program. Events with $Q^2 > 1\text{GeV}^2$ were excluded from the Monte Carlo analysis. In addition, the requirement that $0.2 < y < 0.8$ was imposed.

Samples from the HERWIG and PYTHIA Monte Carlo programs were generated both with and without a simulation of multiparton interactions. In all distributions shown in this work, the minimum $\hat{p}_T$ of the hard scatter has been taken to be 2.5GeV. The parton distribution functions used are the GRV LO [16] for the proton and the WHIT-G [17] for the photon.

8 Definition of Multijet Variables

In 1995, Geer and Asakawa [18] proposed a set of multijet variables which:

1. Span the multijet parameter space.

2. Make it simple to interpret the observed event distributions within the framework of perturbative QCD.

3. Make it easy to compare the characteristics of N-jet events with those of events having (N+1) jets.

This set of variables was chosen by noting that it is possible to completely define a system of N particles in the N-body rest frame by specifying 4N independent parameters. However, momentum conservation provides 3 constraints leaving (4N-3) independent parameters to define the N-body system. In addition, it is possible to rotate the N-body system about the incoming beam direction without losing any interesting information. Consequently, only (4N-4) parameters are required to completely specify the system.

The set of variables consist of the N-body invariant mass and (4N-5) additional variables, each of which is defined in the N-body centre of mass system. For each system, the set of (4N-5) dimensionless variables, along with the multijet mass, span the multijet parameter space and provide a means to compare the properties of multijet events with QCD predictions. In the work presented here, we have studied the set of variables that span the three-jet parameter space. Below, we give a more detailed description of these variables.

8.1 Three-Jet Variables

The three-body rest frame is shown in Figure 6. In this frame, the incoming beam particles are not collinear and so angles are expressed with respect to the average beam direction, $\vec{p_{av}} = \vec{p_1} - \vec{p_2}$, where the incoming particles are labelled 1 and 2, such that $E_1 > E_2$. By convention, the outgoing jets are labelled 3, 4 and 5 such that $E_3 > E_4 > E_5$ where E_i is the energy of jet i in the three-jet rest frame.

The variables of importance to the present analysis are m_{3J}, X_3, X_4, $\cos\theta_3$ and ψ_3, which describe a system of three, massless jets. These parameters are defined as,

1. m_{3J}, the three-jet invariant mass[4],

$$m_{3J} = E_3 + E_4 + E_5 \tag{11}$$

2. X_3, the leading jet energy fraction (normalised),

$$X_3 = \frac{2E_3}{m_{3J}} \tag{12}$$

3. X_4, the next-to-leading jet energy fraction (normalised),

$$X_4 = \frac{2E_4}{m_{3J}} \tag{13}$$

4. $\cos\theta_3$, defined in the three-jet rest frame as the cosine of the leading jet scattering angle,

$$\cos\theta_3 = \frac{\vec{p_{av}}.\vec{p_3}}{|\vec{p_{av}}||\vec{p_3}|} \tag{14}$$

5. ψ_3, defined in the three-jet rest frame as the angle between the three-jet plane and the plane containing the leading jet and the average beam direction,

$$\cos\psi_3 = \frac{(\vec{p_3} \times \vec{p_{av}}).(\vec{p_4} \times \vec{p_5})}{|\vec{p_3} \times \vec{p_{av}}||\vec{p_4} \times \vec{p_5}|} \tag{15}$$

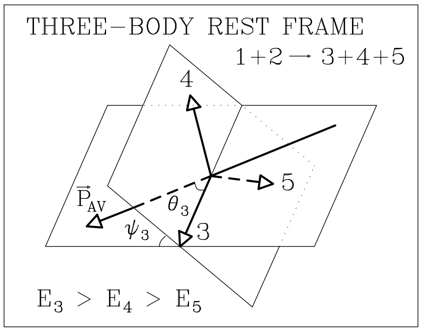

Figure 6: *Schematic definition of angles used to describe the three-jet system in the three-jet rest frame*

[4]In the calculation of the invariant mass, we assume massless single jets.

The quantities X_3 and X_4 are Dalitz variables. A third such variable, X_5, is defined as $X_5 = \frac{2E_5}{m_{3J}}$. X_3, X_4 and X_5 are normalised such that $X_3 + X_4 + X_5 = 2$. Momentum conservation restricts the ranges of the Dalitz variables such that for massless jets $2/3 < X_3 < 1$, $1/2 < X_4 < 1$ and $0 < X_5 < 2/3$. The parameters $\cos\theta_3$ and ψ_3 are angular variables. The variable, θ_3, reflects the orientation of the highest energy jet. However, the variable of most importance to this work is the angle, ψ_3, which reflects the orientation of the lowest energy jet.

9 Definition of the Cross-Section

In this section, we define the region of phase space over which the present study has been carried out.

In the Monte Carlo models, events are required to have at least two jets with $E_T^{jet} > 6$GeV, a third jet with $E_T^{jet} > 5$GeV and jet pseudorapidities in the range $|\eta^{jet}| < 2.4$. Although no accurate energy corrections have yet been performed, it is estimated that jets of hadrons lose about 15% of their energy when passing through inactive material and before impinging on the CAL [2]. Therefore, the corresponding restrictions on the transverse energies of the jets have been reduced by 15% for the data. Although the selection of high transverse energy jets enables perturbative QCD calculations to be applied, it also introduces a bias in the angular distribution by excluding jets produced close to the beam-line. Therefore, to minimise this bias, the constraint $|\cos\theta_3| < 0.8$ has been imposed. In order to increase the proportion of energy available to the third jet, the additional constraint that $X_3 < 0.95$ has been required.

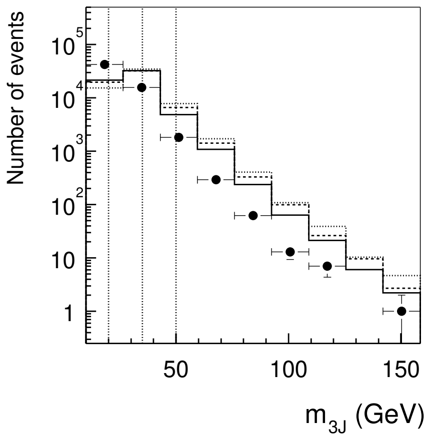

Figure 7: *The distribution of the three-jet invariant mass, for $m_{3J} > 10GeV$, is shown by the black dots where the vertical error bars show the statistical error. The solid and dotted histograms show the predictions from the HERWIG Monte Carlo with and without multiparton interactions, respectively. The dashed histogram shows the PYTHIA prediction with multiparton interactions. The vertical dotted lines indicate the threshold values of the cuts imposed upon the invariant mass of the three-jet system.*

m_{3J} cut	Events passed	E_{T3} (GeV)	E_{T4} (GeV)	E_{T5} (GeV)
$m_{3J} > 10$GeV	60303	9.0	6.9	5.3
$m_{3J} > 20$GeV	42153	10.0	7.4	5.5
$m_{3J} > 35$GeV	5767	15.5	10.8	6.5
$m_{3J} > 50$GeV	970	21.6	15.3	7.9

Table 1: *Number of events passing the three-jet cuts in each of the four kinematic regions. Also shown are the uncorrected, mean transverse energies of the jets found by the KTCLUS algorithm.*

In the current work, we present sets of results corresponding to four different kinematic regions. These regions have been selected by requiring three-jet invariant masses of greater than 10GeV, 20GeV, 35GeV and 50GeV, respectively. The three-jet invariant mass distribution, for events with $m_{3J} > 10$GeV, is shown in Figure 7. The (uncorrected) data are represented by the solid points, the HERWIG Monte Carlo predictions are shown by the solid and dotted histograms (with and without multiparton interactions) and the PYTHIA predictions are shown by the dashed histograms (with multiparton interactions). The distribution falls approximately exponentially from the threshold values, which are indicated by the vertical dotted lines, to the highest measured value of $m_{3J} \approx 150$GeV. Each Monte Carlo model distribution has been scaled to the number of events passing the three-jet cuts, which are given in Table 1. Also shown in Table 1, are the uncorrected, mean transverse energies of the jets, following imposition of the cuts.

10 Results and Discussion

In this section, the distributions of the set of variables which span the multijet parameter space for three, massless jets are presented. In each diagram, the data are represented by the solid points, the HERWIG Monte Carlo predictions are shown by the solid and dotted histograms (with and without multiparton interactions) and the PYTHIA Monte Carlo predictions are shown by the dashed histograms (with multiparton interactions). All distributions have been area normalised. As yet, no fixed-order perturbative QCD calculations have been performed and the data have not yet been corrected for detector effects. Consequently, the comparison between data and Monte Carlo is for illustrative purposes and should not be considered as an accurate measurement.

The distributions of the energy-sharing quantity, X_3, are shown in Figures 8(a) to 11(a). In Figures 8(a) and 9(a), a comparison of the HERWIG Monte Carlo models with and without multiparton interactions indicates some sensitivity to multiple scattering. In particular, the model distributions where multiparton interactions have been included show a significant depletion at high X_3, compared to those models where multiple scattering has not been included. However, the PYTHIA distribution does not appear to follow this same trend. Although the data are not accurately described by any model at high X_3 there appears, in general, to be a strong tendency to follow the HERWIG distributions where multiparton interactions have been included. The distributions of X_3, for invariant masses greater than 35GeV and 50GeV, are shown in Figures 10(a) and 11(a),

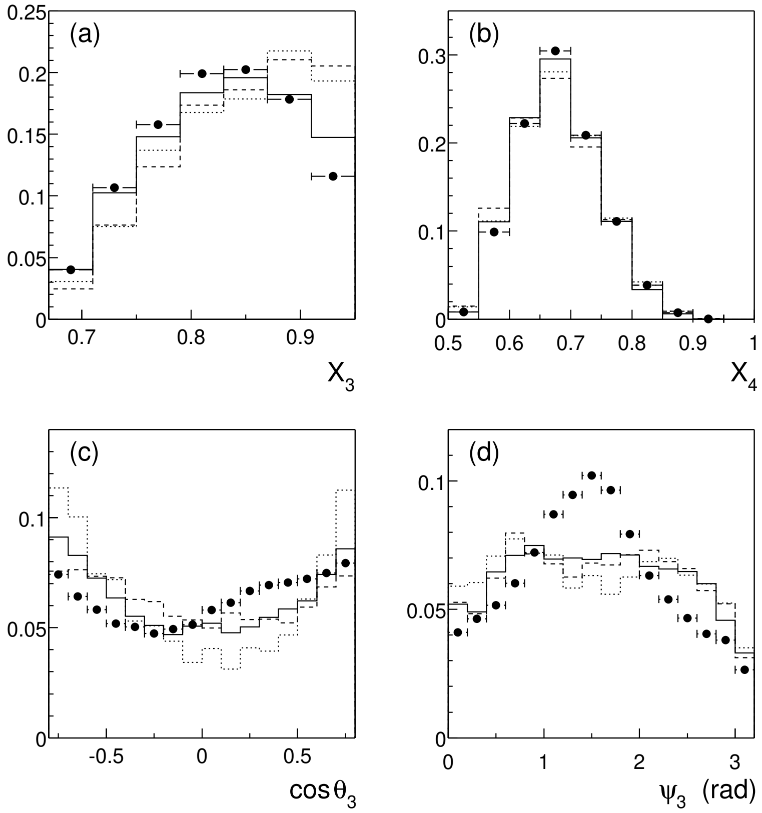

Figure 8: *The distributions of the energy sharing quantities X_3 and X_4, are shown by the black dots in* (a) *and* (b)*, respectively, and the distributions of* $\cos\theta_3$ *and* ψ_3 *are shown in* (c) *and* (d)*, for a three-jet invariant mass of greater than 10GeV. The vertical error bars show the statistical error. The solid and dotted histograms show the predictions of the HERWIG Monte Carlo with and without multiparton interactions. The dashed histogram shows the prediction from the PYTHIA Monte Carlo with multiparton interactions.*

respectively. The distributions show that in these, higher energy, regimes the distinction between models with and without multiparton interactions becomes less obvious. In both sets of diagrams, the distributions of the data are reasonably well described by models both with and without multiple scattering.

The distributions of the variable, X_4, are shown in Figures 8(b) to 11(b). According to the Monte Carlo models, this quantity shows little sensitivity to multiple parton scattering. However, the shape of the data is well described by the models both with and without a simulation of multiple scattering included, particularly in the lower energy regimes.

The distributions of $\cos\theta_3$ are shown in Figures 8(c) to 11(c). In Figure 8(c), which shows the distribution for invariant masses greater than 10GeV, the Monte Carlos indicate a high sensitivity to multiparton interactions, with the distributions for models with multiple scattering included being significantly less peaked in the forward and backward directions. The data are not well described by any of the Monte Carlo models at this stage. However, there appears to be an obvious trend away from the model without multiparton interactions. The distributions of $\cos\theta_3$, for three-jet invariant masses of 20GeV, 35GeV

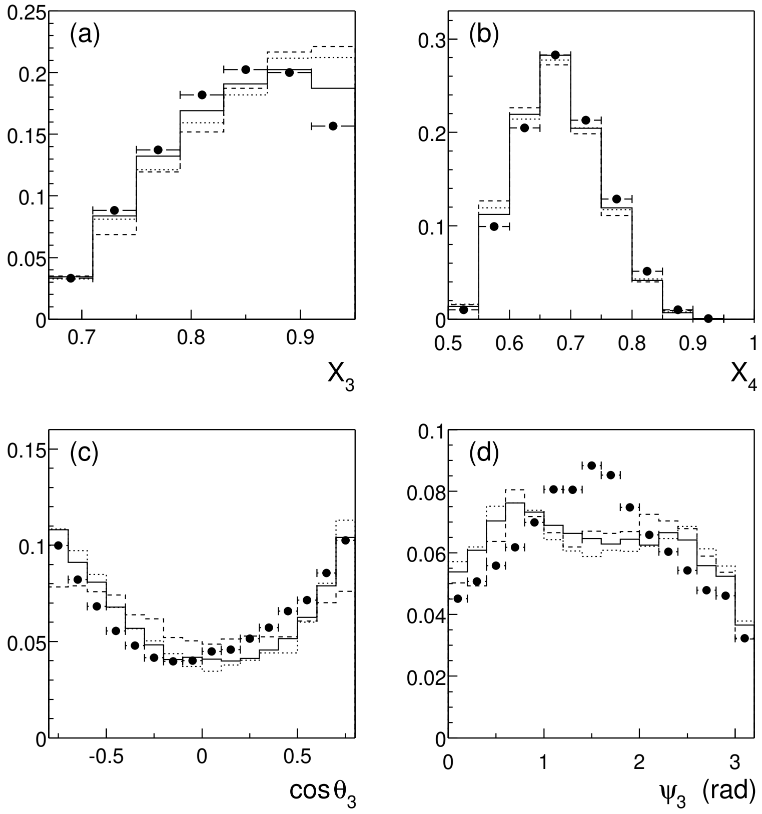

Figure 9: *The distributions of the energy sharing quantities X_3 and X_4, are shown by the black dots in* (a) *and* (b)*, respectively, and the distributions of* $\cos\theta_3$ *and* ψ_3 *are shown in* (c) *and* (d)*, for a three-jet invariant mass of greater than 20GeV. The vertical error bars show the statistical error. The solid and dotted histograms show the predictions of the HERWIG Monte Carlo with and without multiparton interactions. The dashed histogram shows the prediction from the PYTHIA Monte Carlo with multiparton interactions*

and 50GeV are shown in Figures 9(c), 10(c) and 11(c), respectively. The distinction between the HERWIG Monte Carlos with and without multiparton interactions becomes much less apparent in the kinematic regimes corresponding to these diagrams. In both the HERWIG and PYTHIA models, the forward and backward peaks, which are expected in perturbative QCD, are more pronounced than in the diagram corresponding to the lowest energy regime. However, the PYTHIA distributions show a distinct depletion in the forward and backward directions compared to those of HERWIG. In Figures 9(c) and 10(c), the general trend of the data is reasonably well described by the HERWIG models both with and without multiparton interactions. However, there appears to be a slight asymmetry in the data. This may simply be due to detector effects which have not yet been taken into account. In Figure 11(c), the data are less well described by the Monte Carlo models, particularly in the forward direction. However, this may be largely due to the limited statistics in the highest energy region.

The most important distribution for the focus of this report is that of the variable, ψ_3, which reflects the orientation of the lowest energy jet in a three-jet event. The distributions of this variable, for three-jet invariant mass cuts of 10GeV and 20GeV, are shown in

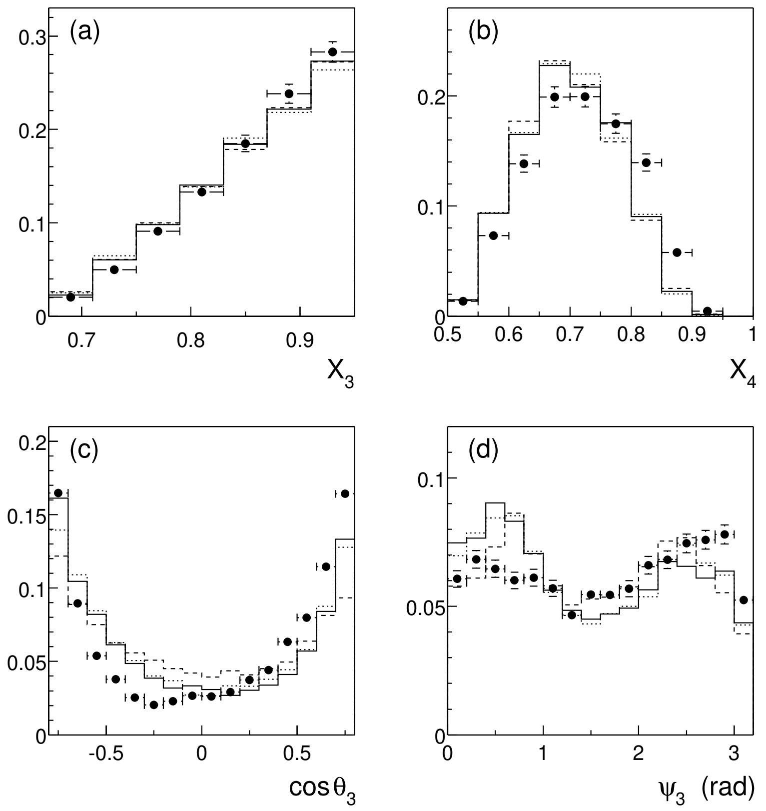

Figure 10: *The distributions of the energy sharing quantities X_3 and X_4, are shown by the black dots in* (a) *and* (b)*, respectively, and the distributions of* $\cos\theta_3$ *and* ψ_3 *are shown in* (c) *and* (d)*, for a three-jet invariant mass of greater than 35GeV. The vertical error bars show the statistical error. The solid and dotted histograms show the predictions of the HERWIG Monte Carlo with and without multiparton interactions. The dashed histogram shows the prediction from the PYTHIA Monte Carlo with multiparton interactions*

Figures 8(d) and 9(d), respectively. Comparison of the Monte Carlo models shown in these figures, for events with and without multiparton interactions, indicates a strong sensitivity to multiple scattering. The jet algorithm and minimum transverse energy requirements for the jets, deplete the distributions near $\psi_3 \sim 0$ and π. However, with this taken into account, the models without multiparton interactions show a strong tendency for the three-jet plane to lie close to the plane containing the beam and the highest energy jet. However, in models where multiple scattering has been included, this effect becomes much less obvious and we observe a flattening of the ψ_3 distribution. This is particularly apparent in the diagram corresponding to the lowest energy region. This effect indicates a trend towards a uniform population of the available phase space (as can be inferred from a comparison with the phase space distribution shown in Figure A2(d)). Since a second scatter is independent of the primary hard interaction, the orientation of a third jet arising from multiple parton scattering, with respect to the primary jets, should be random in phase space. Hence, an observation of a flattening in the measured ψ_3 distribution at low invariant masses would be evidence for multiple parton scattering. In this kinematic regime, the data show no peaks towards $\psi_3 \sim 0$ and π. Although there exist significant

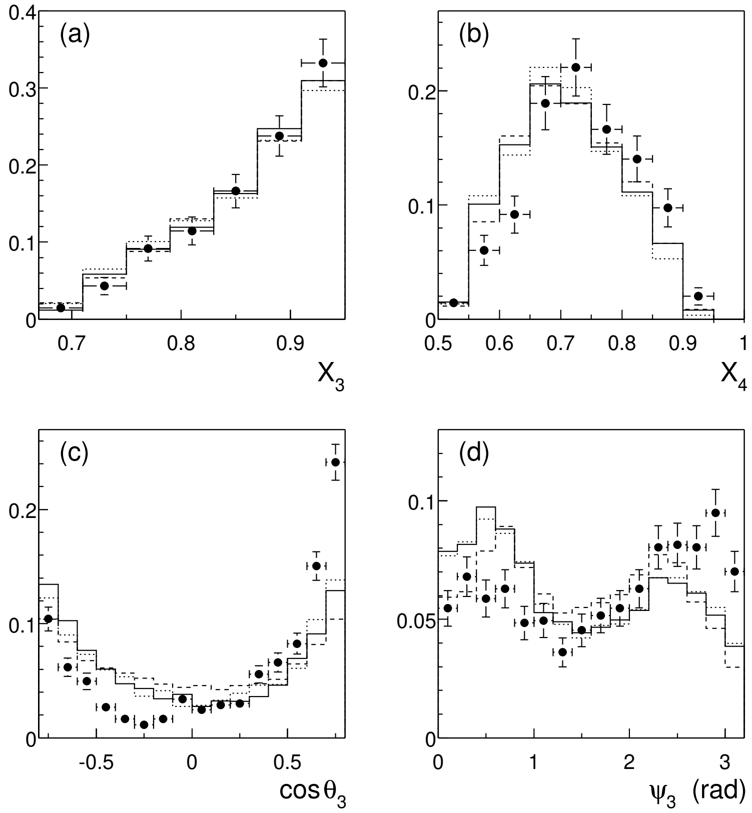

Figure 11: *The distributions of the energy sharing quantities X_3 and X_4, are shown by the black dots in* (a) *and* (b)*, respectively, and the distributions of* $\cos\theta_3$ *and* ψ_3 *are shown in* (c) *and* (d)*, for a three-jet invariant mass of greater than 50GeV. The vertical error bars show the statistical error. The solid and dotted histograms show the predictions of the HERWIG Monte Carlo with and without multiparton interactions. The dashed histogram shows the prediction from the PYTHIA Monte Carlo with multiparton interactions*

discrepancies between data and Monte Carlo, this preliminary comparison suggests that the distributions may be significantly better described by models where multiple parton scattering has been included. In contrast, the ψ_3 distributions for invariant mass cuts of 35GeV and 50GeV are shown in Figures 10(d) and 11(d). In these figures, the distinction between models with and without multiparton interactions is much less obvious. At this stage, the data are not well described by any of the Monte Carlo models, particularly in the region towards $\psi_3 \sim 0$. This may be due to detector effects. However, despite the apparent discrepancies, the data show prominent peaks towards $\psi_3 \sim 0$ and π. This suggests that, in the higher energy regimes, a strong correlation exists between the orientation of the lowest energy jet and that of the leading jet. This indicates that, as expected, in the higher energy regimes the third jet will arise predominantly from the parton shower and will not be due to a second scatter.

11 Summary

The distributions of the set of variables which span the three-jet parameter space have been presented for four different kinematic regimes. As expected, the Monte Carlo models indicate little sensitivity to multiparton interactions in the high energy regimes. However, in the lower energy regions, the three-jet angular distributions show a strong sensitivity. Of particular interest is the variable, ψ_3, which reflects the orientation of the lowest energy jet in a three-jet event. As found by the ZEUS Collaboration, the distribution of this variable in the high energy region suggests that the third jet arises from the parton shower and is not due to a second hard scatter. However, the work presented here shows that, at low invariant masses, the model distributions of this variable show a distinct flattening. This indicates a tendency towards a uniform population of phase space, as would be expected if a significant proportion of events have a third jet arising from a second scatter. The effects observed in the models are significant enough to be measured with the ZEUS detector. A preliminary comparison with the data suggests that, in the lower energy regime, the measured distributions may be significantly better described by models where multiparton interactions have been included.

12 Future work

Plans for the immediate future focus mainly on the work presented in this report. In addition, a similar analysis is currently being performed for events containing at least four, high transverse energy jets. As indicated in previous sections, the set of multijet variables can be extended to four or more jets. The interpretation of the four-jet variables, in the context of the effects of multiparton interactions on the measured distributions, is not as simple as for the three-jet case. For this reason, and due to restrictions on the size of this report, this work has not been discussed here. However, the status of the four-jet analysis is currently at the same stage as for the study of three-jet events presented in this report. Therefore, immediate plans focus on the completion of the measurement of both the the three and four-jet inclusive cross-sections. This will involve several stages. In order to complete the measurements, it is necessary to carry out jet-energy and acceptance corrections on the data. Performing jet-energy corrections involves using Monte Carlo samples to determine the energy losses suffered by the jets when passing through inactive material. The calculation of acceptance corrections involves determining the inefficiencies of the trigger and offline selection cuts as well as the migrations caused by detector effects. A calculation of systematic errors must also be performed. Once the measurement is complete, it will need to be analysed in greater detail than in the present report. The distributions shown in previous sections must be compared with fixed-order perturbative QCD calculations and the accuracy of the description of the data by both these calculations and the parton shower models must be assessed.

Appendix A

A Overview of Previous Three-Jet Cross-Section Measurement

In this section, we give an overview of the ZEUS Collaboration measurement of the inclusive cross-section for the photoproduction of events containing at least three jets with a three-jet invariant mass of $m_{3J} > 50\text{GeV}$ [2]. The measurement was made for events having at least two jets with $E_T^{jet} > 6\text{GeV}$ and a third jet with $E_T^{jet} > 5\text{GeV}$ where each of the three jets was required to satisfy $|\eta^{jet}| < 2.4$.

As has been discussed in previous sections, the requirement of high transverse energy jets introduces a bias in the angular distributions. Therefore, the additional requirements that $|\cos\theta_3| < 0.8$ and $X_3 < 0.95$ were imposed. Following these cuts, it was found that the mean transverse energy of the highest, the second highest and the third highest transverse energy jets were approximately 20GeV, 15GeV and 10GeV, respectively.

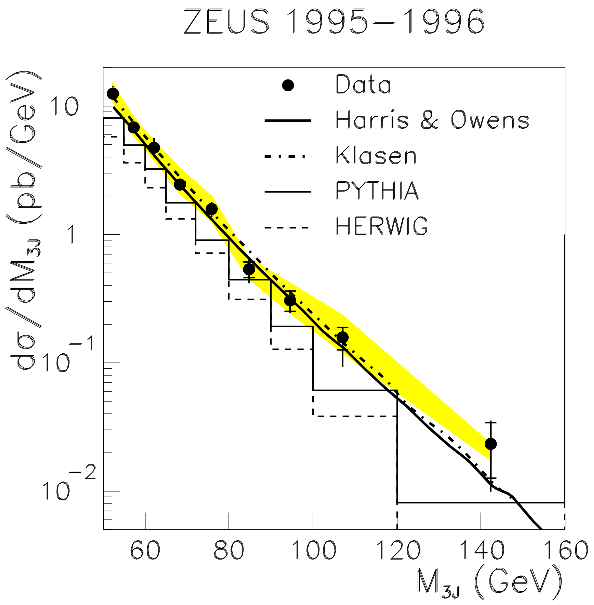

Figure A1: *The ZEUS Collaboration measurement of the three-jet cross-section with respect to the three-jet invariant mass, $d\sigma/dm_{3J}$, is shown by the black dots where the inner error bar shows the statistical error and the outer error bar is the sum, in quadrature, of the statistical error and the systematic uncertainty. The jet-energy scale uncertainty, which is highly correlated between bins, is shown separately as the shaded band. $O(\alpha\alpha_s^2)$ perturbative QCD calculations by Harris & Owens and Klasen are shown by the thick solid and dot-dashed lines, respectively. The thin solid and dashed histograms show the predictions from two different parton shower models, HERWIG and PYTHIA.*

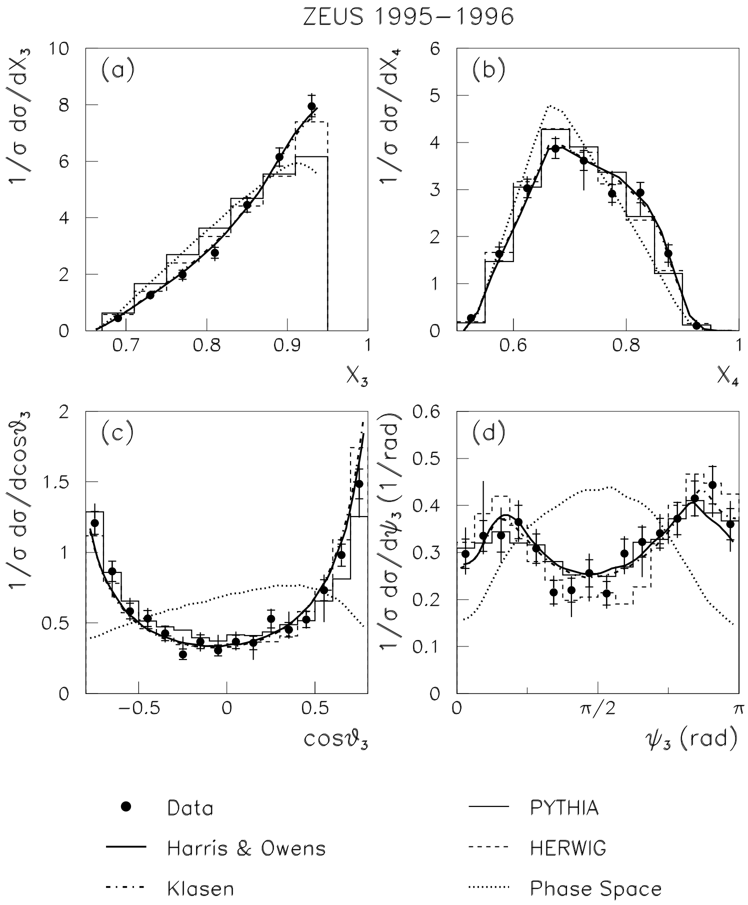

Figure A2: *The distributions of the energy sharing quantities,* X_3 *and* X_4*, are shown by the black dots in* (a) *and* (b)*, respectively, and the distributions of the* $\cos\theta_3$ *and* ψ_3 *are shown in* (c) *and* (d)*. Inner error bars show the statistical error and the outer error bars show the quadratic sum of this with the systematic uncertainty. The fixed-order perturbative QCD predictions are shown by the thin solid and dashed histograms. The phase-space distribution of three jets is indicated by the dotted line.*

The ZEUS Collaboration measurement of the three-jet inclusive cross-section, with respect to the three-jet invariant mass, and of the three-jet variables X_3, X_4, $\cos\theta_3$ and ψ_3 are shown in Figures A1 and A2. In each diagram, the data is represented by the solid points, the fixed order perturbative QCD predictions are shown by the thick solid and dot-dashed lines and the parton shower model predictions are shown by the thin solid and dashed histograms. The phase space distributions of events containing three jets, for events satisfying $m_{3J} > 50$GeV, are indicated by the dotted lines.

The three-jet invariant mass distribution, shown in Figure A1, indicates that the cross-section falls exponentially from the threshold value of $m_{3J} = 50$GeV up to the highest measured value of $m_{3J} \approx 150$GeV. The data are compared with two different $\mathcal{O}(\alpha\alpha_s^2)$ perturbative QCD calculations and the predictions are found to be in good agreement with the data. In addition, the m_{3J} distribution predicted by the HERWIG and PYTHIA

Monte Carlos, agree with the data in shape although the predicted cross-sections appear to be too low by $\sim 30 - 40\%$.

The distributions of the fraction of the available energy taken by the highest and second highest transverse energy jets are shown in Figures A2(a) and (b), respectively. The parton shower models give a reasonable description of these energy sharing quantities, as do the perturbative QCD calculations. However, the similarities between the measured distributions and the three-body phase space predictions indicate that the distributions have minimal sensitivity to the perturbative QCD matrix elements.

The $\cos\theta_3$ and ψ_3 distributions are shown in Figures A2(c) and (d). The $\mathcal{O}(\alpha\alpha_s^2)$ perturbative QCD calculations and the parton shower models are both in good agreement with the data. However, the measured angular distributions are dramatically different from those obtained assuming a uniform population of phase space. This demonstrates that these quantities are especially sensitive to the perturbative QCD matrix elements.

In the kinematic regime studied by the ZEUS Collaboration, it was found that including a simulation of multiparton interactions in the HERWIG and PYTHIA programs had no significant effect on the three-jet cross-section or the angular distributions generated. Consequently, it was concluded that, in this energy regime, the third jet arises from the parton shower and is not due to a second hard scatter. In contrast, the work carried out in this report, shows that in lower energy regimes, the effects of multiparton interactions may be significant.

Appendix B

B Detailed Event Reconstruction

In this section we look, in more detail, at the ways in which the kinematic variables important to photoproduction are reconstructed. As stated in previous sections, these quantities are not directly measurable and so must be reconstructed from quantities that can be determined experimentally.

B.1 Reconstruction of y and Q^2

There are many methods by which to reconstruct the variables y and Q^2 [19]. In this section we discuss the "electron method" and the "Jacquet-Blondel" method.

B.1.1 The Electron Method

Both y and Q^2 can be calculated using the momenta of the scattered electron or positron as,

$$y_e = 1 - \frac{E'_e}{2E_e}(1 - cos\theta_e) \tag{B1}$$

$$Q^2_e = 2E_eE'_e(1 + cos\theta_e) \tag{B2}$$

where E_e and E'_e are the incoming and scattered lepton energies respectively and θ_e is the scattered lepton angle with respect to the proton beam direction. Since θ_e is large in the low Q^2 events that we have been discussing in this report, the lepton will continue to travel in a direction close to its original path. Therefore, substituting large values of θ_e into (B1) gives that, $y_e = \frac{(E_e - E'_e)}{E_e} \approx \frac{E_\gamma}{E_e}$. Therefore, y simply becomes the fraction of the electron energy carried by the exchanged photon.

B.1.2 The Jacquet-Blondel Method

Another approach for reconstructing y and Q^2 is the Jacquet-Blondel method which uses the hadronic final state. In this case, y is reconstructed from energy deposits in the calorimeter. Summing over all final state partons, except for the lepton, gives

$$y_{JB} = \frac{\sum_i (E_i - p_{zi})}{2E_e} \tag{B3}$$

$$Q^2_{JB} = \frac{(\sum_i p_{xi})^2 + (\sum_i p_{yi})^2}{1 - y_{JB}} \tag{B4}$$

The sum runs over all cells of the UCAL except when the scattered lepton enters the detector. In such events, cells belonging to the cluster and identified as being caused by the scattered lepton are excluded from the sum. If it is not possible to remove such cells, as in the case of low energy electrons which have not been identified by the electron-finder, then values of y_{JB} which approach unity will be observed.

The angular position of each cell is determined from the nominal cell centre corrected for the position of the event vertex as reconstructed from tracks in the ZEUS CTD. This definition is relatively insensitive to loss of particles down the forward beam-pipe.

B.2 Reconstruction of x_p and x_γ

At leading order, the fractional momenta carried by the incoming partons of both the proton and the photon can be reconstructed from the final state jet kinematic variables. Conservation of energy and momenta give,

$$x_p^{LO} = \frac{\sum_{partons} E_T^{parton} \exp\left(\eta^{parton}\right)}{2E_p} \tag{B5}$$

$$x_\gamma^{LO} = \frac{\sum_{partons} E_T^{parton} \exp\left(-\eta^{parton}\right)}{2E_\gamma} \tag{B6}$$

where E_T^{parton} and η^{parton} are the transverse energy and pseudorapidity of the outgoing partons from the hard scatter. Since for low Q^2 events, $y \approx \frac{E_\gamma}{E_e}$ then (B6) can be written as,

$$x_\gamma^{LO} = \frac{\sum_{partons} E_T^{parton} \exp\left(-\eta^{parton}\right)}{2yE_e} \tag{B7}$$

In this simple, leading order picture and using this definition, direct photoproduction events contribute purely at $x_\gamma^{LO} = 1$, whilst resolved events populate the region at lower x_γ^{LO}.

However, since parton energies are not measurable, we need to be able to construct x_p and x_γ from quantities which can be determined experimentally. For those events in which two jets are observed in the detector, it is possible to estimate the fraction of the photon and proton momenta which participate in the hard process by replacing the sum over partons in (B5) and (B6) with a sum over the jets. At higher order, the situation is more complicated. Similarly, in events where the photon remnant carries non-negligible transverse energy, we may observe additional jets. For this reason, the following operational definitions of x_p and x_γ are defined, where the sum is over only the two jets of highest transverse energy,

$$x_p^{OBS} = \frac{\sum_{jets1,2} E_T^{jet} \exp\left(\eta^{jet}\right)}{2E_p} \tag{B8}$$

$$x_\gamma^{OBS} = \frac{\sum_{jets1,2} E_T^{jet} \exp\left(-\eta^{jet}\right)}{2yE_e} \tag{B9}$$

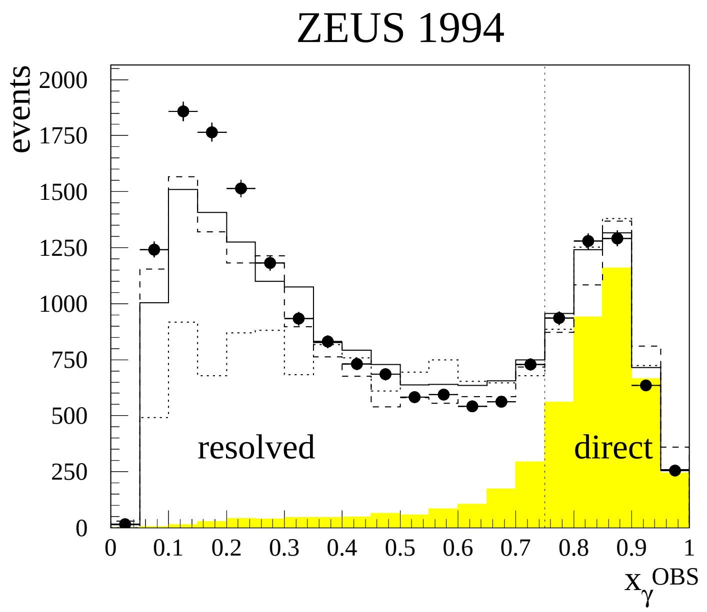

Figure B1: *The x_γ^{OBS} distribution for dijet events for the 1994 data (black dots) compared with the HERWIG both with and without multiparton interactions (solid line and dotted line) and the PYTHIA with multiparton interactions (dashed line) Monte Carlo generators. The shaded area represents the contribution due to direct photoproduction processes as generated by HERWIG. The vertical line is the experimental cut used to separate direct and resolved processes.*

In this case x_p^{OBS} and x_γ^{OBS} are the fraction of the incoming proton and photon energies which participate in the production of the two highest E_T jets. Providing that all events are treated consistently in both experiment and in theoretical calculations, the above definition of x_p^{OBS} and x_γ^{OBS} are valid. This is defined to all orders of perturbation theory.

Due to complications at higher orders and due to hadronisation and parton shower effects, the direct contribution in the data will not lie at exactly $x_\gamma = 1$. However, it is still possible to choose a working experimental definition for direct and resolved photoproduction. It is usual to define direct events to be those with $x_\gamma^{OBS} > 0.75$ and resolved to be those with $x_\gamma^{OBS} < 0.75$. The distribution of x_γ^{OBS} and the experimental cut used to distinguish between direct and resolved events are shown in Figure B1.

Appendix C

C Jet Algorithms

A jet is not a fundamental QCD object. Therefore, it is necessary to find an exact definition of a jet. There are many ways to define a jet in both theory and experiment. However, there are generally considered to be two constraints on the exact definition, as follows,

- Firstly, the same results should be obtained for the classification of any given event and an exactly similar event but with an arbitrary number of infinitely soft partons with arbitrary directions added to it. Another way of saying this is that the results should not be influenced by the emission of very low energy particles. This is known as *infrared safety.*

- Secondly, the same results should be obtained for the classification of any event and an exactly similar event but with any massless partons replaced by an arbitrary number of infinitely collinear, massless partons with the same total momentum. This is known as *collinear safety.*

If either of these conditions is violated, even for some small class of events, the results will be divergent in perturbation theory indicating that they are fundamentally non-perturbative. It is, therefore, necessary to create an algorithm which can identify jet-like objects whilst satisfying the conditions defined above.

Within the ZEUS collaboration, use is made of two types of jet algorithm for photo-production analysis; namely, the cone and cluster algorithms. Two variants of the cone type are used (EUCELL [11] and PUCELL [12]) whilst the cluster algorithm used is the k_T [8] algorithm as implemented in the KTCLUS library of routines [9]. Each of these algorithms can be used at the calorimeter, hadron or parton level. Below we give a brief overview of each type of algorithm.

C.1 Cone Algorithms

The two cone algorithms typically used within the ZEUS collaboration are defined in accordance with the Snowmass Convention [20]. The Snowmass Convention defines the jet recombination scheme for the transverse energy and jet direction as,

$$E_T^{jet} = \sum_i E_{t,i} \tag{C1}$$

$$\eta^{jet} = \frac{1}{E_T^{jet}} \sum_i E_{t,i}\eta_i \tag{C2}$$

$$\phi^{jet} = \frac{1}{E_T^{jet}} \sum_i E_{t,i}\phi_i \tag{C3}$$

where the sum runs over all hadrons or calorimeter cells within the jet cone. By definition, jets from a cone algorithm have a maximal radius of R in $\eta - \phi$ space and at each stage of the jet forming, a particle i is combined with the jet if,

$$\Delta R^2 = [(\eta_i - \eta_{jet})^2 + (\phi_i - \phi_{jet})^2] \leq R^2_{cone}$$

In general, a radius of $R_{cone} = 1$ is generically taken for the cone algorithms mentioned here, although the detailed properties of jet merging and seed finding are not defined within the Snowmass Convention and may be different for each jet algorithm. This means that jets from different cone algorithms with identical cone radii need not coincide. Both EUCELL and PUCELL use the concept of pre-clustering, although they are different in terms of their implementation and treatment of overlapping jets.

In EUCELL, clusters are determined using a grid in $\eta - \phi$ space. The size of the cells that make up the grid is determined such that $\Delta\eta^{gridcell} \approx \Delta\phi^{gridcell} \approx R/2$. By then sliding a 3×3 cell window over the grid, a potential pre-cluster is formed. Pre-clusters are required to have a transverse energy above some prescribed lower cut-off. A cone of radius R is then placed around the pre-cluster and an iterative process is performed. The first jet is defined as the cone with the highest transverse energy. Successive jets are then determined from the remaining objects by the same procedure until there exist no more cones above the energy threshold.

PUCELL is an adaption of the jet algorithm used within the CDF collaboration. A pre-cluster is formed by combining all objects within a radius, R, with the highest E_T object. This is done until all objects are assigned to a pre-cluster. The centre of the pre-clusters are then recalculated and the process repeated until a stable state, or maximum number of iterations, is reached. The formation of clusters is then complete and those that have a transverse energy above a certain threshold are considered to be jets.

C.2 Clustering Algorithms

Cone algorithms have several limitations and can lead to ambiguities. For example, the treatment of overlapping jets is not defined within the Snowmass Convention, and neither is the question of seed finding for the initial jets. This leads to theoretical ambiguity with respect to jet merging in the final state and the process is not infrared safe above next-to-leading order (NLO) without modification.

These problems are avoided by use of the k_T algorithm, as the merging criterion is completely defined for any given final state. Hence, in all work presented here, we have avoided the problems inherent in the use of the cone algorithm by using only the k_T algorithm.

The k_T algorithm was initially designed for use in e^+e^- annihilation [21]. However, the presence of hadron remnants in hadron-hadron, DIS or photoproduction events means that it must be used in a modified form which maintains the property of factorisation of initial state radiation [9].

For a cluster algorithm we must specify some distance measure which determines *which* particles will be merged together with a recombination scheme which defines *how* they will be merged. In photoproduction the algorithm is run in the laboratory frame using the inclusive recombination scheme of Ellis and Soper [10] in a mode which is invariant under longitudinal boosts. The recombination scheme is similar to that of the Snowmass convention (the so-called p_T mode). The algorithm scheme depends on a parameter R, which is analogous to a cone radius.

To decide which particles should be merged, the following quantity is formed for each particle i,

$$d_i = E_{t,i}^2$$

and for each pair of particles, ij, we form the quantity,

$$d_{ij} = \min(E_{t,i}^2, E_{t,j}^2)[(\eta_i - \eta_j)^2 + (\phi_i - \phi_j)^2]/R^2$$

The d_i is the limiting case of small angles of the "distance" between particle i and a large mass remnant travelling along the z-direction.

If the smallest of all the d values is d_{ij}, then particles i and j are merged into a single object, k. However, if the smallest value is a d_i then this particle is considered "complete" and is removed from further clustering. This process is then repeated until all the objects have been removed, producing an E_T ordered list of objects.

The scheme for merging the objects is similar to the Snowmass convention and is given by,

$$E_{t,ij} \equiv E_{t,i} + E_{t,j} \tag{C4}$$

$$\eta_{ij} \equiv \frac{E_{t,i}\eta_i + E_{t,j}\eta_j}{E_{t,ij}} \tag{C5}$$

$$\phi_{ij} \equiv \frac{E_{t,i}\phi_i + E_{t,j}\phi_j}{E_{t,ij}} \tag{C6}$$

Therefore, the scheme assigns objects to jets in a well-prescribed manner, and since each quantity E_T, $\Delta\eta$, $\Delta\phi$ in the distance parameter are invariant under longitudinal boosts, so the property of boost invariance of the jet finding itself is retained.

Appendix D

D Implementation of Monte Carlo Event Generators

In this section we describe the implementation of both the HERWIG and PYTHIA Monte Carlo event generators. In particular, we focus on the manner in which the treatment of multiparton interactions is formulated.

D.1 The HERWIG Generator

The Hadron Emission Reactions With Interfering Gluons (HERWIG) Monte Carlo is a general purpose generator which attempts to provide as complete an implementation of the LO perturbative QCD processes as possible. The aim is to describe the largest possible number of processes with the fewest possible number of free parameters. Particular attention is paid to being as independent as possible from non-perturbative parameters. Consequently, HERWIG has a very large predictive power.

HERWIG generates the entire partonic structure of a given event from the hard subprocess. The factorisation scale for the hard subprocess, μ^2, is given by,

$$\mu^2 = \tfrac{2\hat{s}\hat{t}\hat{u}}{\hat{s}^2+\hat{t}^2+\hat{u}^2}$$

where $\hat{s}$, $\hat{t}$, $\hat{u}$ are the Mandelstam variables. In the limit of massless partons and scattering perpendicular to the beam axis, μ^2 is the same as $\frac{4}{3}\hat{p}_T^2$. The cross-section is divergent in the limit $\hat{p}_T \rightarrow 0$, and so a minimum transverse momentum cut, $\hat{p}_T^{min}$, is introduced.

In HERWIG, the incoming and outgoing partons undergo a showering process in which hadrons are formed from the partons. This showering is initiated by each individual parton splitting into many partons. Logarithms of the form $(\alpha_s \log(\mu^2/\mu_o^2))^n$ are resummed and the partons ordered such that, at each branching, the angle between the two partons is smaller than that at the previous branching. This ordering is continued until the hadronisation scale is of the order of the mass of the lightest mesons.

The treatment of parton showers from the initial hadrons is different to that of the partons from the hard subprocess. In the initial state, the chain of radiation evolves backwards from the hard subprocess to the incoming hadrons until some cut-off is reached. At each point in the cascade, the partons have an equivalent x and Q^2, and the type of partons produced are consistent with the chosen parton distribution function parameterisation for this x and Q^2.

For resolved photoproduction, HERWIG begins by generating the radiated photon from the incoming electron using the Equivalent Photon Approximation (EPA). At each stage, the backwards evolution allows the possibility for a $\gamma \rightarrow q\bar{q}$ vertex in resolved events. For direct events, the full $2 \rightarrow 3$ matrix elements for scattering are used.

When the scale of the outgoing parton shower has reached the mass of the light mesons, the transition from partons to hadrons proceeds via a non-perturbative model called the cluster model. This exploits the *pre-confinement* property of QCD where partons are grouped into colour neutral objects. This is done by splitting all the gluons into $q\bar{q}$ pairs. These quarks are then clustered into colourless objects via the colour connections generated in the parton shower. Each cluster is then fragmented into two hadrons or the lightest meson for its flavour if the cluster is not massive enough to produce two hadronic objects. Finally, the decay of unstable particles is simulated.

D.1.1 Implementation of Multiparton Interactions in HERWIG

The formulation for multiparton interactions that is followed in HERWIG begins by considering the scattering of two overlapping hadronic objects. It is assumed that the partons taking part in the interaction are distributed according to the electric form factors of the hadrons, where the form factor of the pion is used for the photon. From the Fourier transform of the product of the two form factors it is possible to obtain the overlap function, $A(b)$, which gives the relative density of the parton content of the two hadrons where they overlap, for a scatter with impact parameter, b. Multiplying this with the parton density functions gives the partonic luminosity for a photon-proton collision with this impact parameter,

$$d\mathcal{L} = A(b) f^P(x_P) \frac{f^\gamma(x_\gamma)}{P_{res}} dx_\gamma dx_p \tag{D1}$$

The factor P_{res} is the probability that the photon fluctuates into the hadronic state with parton density $f^\gamma(x_\gamma)$. In the simulation this factor is ignored, since for any particular interaction the photon has either fluctuated or it has not. The partonic luminosity integrated over all impact parameters must simply be equal to the product of the parton density functions, hence $\int A(b)\pi d^2b = 1$. The average number of partonic interactions in photon-proton interactions with impact parameter b is then:

$$n(b) = \int_{\hat{p}_T^{min\,2}}^{W^2/4} \int\int A(b) f^p(x_p) \frac{f^\gamma(x_\gamma)}{P_{res}} \frac{d\hat{\sigma}^{ab\to cd}}{d\hat{p}_T^2} dx_p dx_\gamma d\hat{p}_T^2 \tag{D2}$$

$$n(b) = \frac{A(b)}{P_{res}} \sigma_{QCD}^{\gamma p}(\hat{p}_T^{min\,2}) \tag{D3}$$

The probability of there being m partonic interactions is,

$$P_m(b) = \frac{\langle n(b)\rangle^m}{m!} \exp(-\langle n(b)\rangle) \tag{D4}$$

Taking the sum of all probabilities for $m = 1 \to \infty$ and integrating over b gives the total non-diffractive (ND) photon-proton cross-section,

$$\sigma_{ND}^{\gamma p} = P_{res} \int \Sigma_{m=1}^{\infty} P_m(b) \pi d^2b = \pi P_{res} \int [1 - \exp(-\langle n(b)\rangle)] d^2b \tag{D5}$$

Thus, by using the form factors and P_{res} the total non-diffractive photon-proton cross-sections for $\hat{p}_T > \hat{p}_T^{min}$ can successfully be calculated. The result of this method strongly depends upon the value of $\hat{p}_T^{min}$, and the calculation can always be brought into agreement with a measurement at a particular centre of mass energy, W, using a suitable choice of $\hat{p}_T^{min}$. However, this approach does make a real prediction of the W dependence of the cross-section. The choice of $\hat{p}_T^{min}$ is always bound up with the particular structure function being used, and for different combinations of parameterisations of photon and proton structure functions, there are various optimal values of $\hat{p}_T^{min}$.

The average number of partonic interactions per event, calculated using this model, is,

$$\langle n\rangle = \frac{\int \Sigma_{m=1}^{\infty} m P_m d^2b}{\int \Sigma_{m=1}^{\infty} P_m d^2b} = \frac{\int \langle n(b)\rangle d^2b}{\int [1-\exp(-\langle n(b)\rangle)] d^2b} = \frac{\sigma_{QCD}^{\gamma p}}{\sigma_{ND}^{\gamma p}} \tag{D6}$$

HERWIG uses the above method to calculate the probability of finding m partonic scatters in an event with photon-proton centre of mass energy W, where a Poisson distribution about the average value found from equation (D6) is assumed.

No explicit impact parameter dependence is used. From this probability distribution, the number of partonic interactions, m, is determined for each event. Each one of these scatters is generated according to the QCD cross-section,

$$\frac{d^3\sigma_{QCD}^{\gamma p}}{dx_\gamma dx_p d\hat{p}_T^2}(x_\gamma, x_p, \hat{p}_T^2) \tag{D7}$$

In HERWIG, the value of $\hat{p}_T^{min}$, once selected, is used for both the primary partonic interaction and all secondary interactions.

The fact that the partons all come from a common parent hadron is dealt with by stopping the production of further scatters as soon as such a scatter would require a parton to take more of the proton or photon energy than remains after the preceding scatter.

D.2 The PYTHIA Generator

Like HERWIG, PYTHIA is a general purpose Monte Carlo generator. The simulation of an event is divided into the same stages as for HERWIG. However, there are also significant differences between the two generators. There are two main differences in the perturbative phases of the respective models. Firstly, in photoproduction events, the photon spectrum in PYTHIA is generated using the Weizäcker-Williams Approximation (WWA) for both direct and resolved photon processes. Secondly, the factorisation scale used, μ^2, is the transverse mass of the two outgoing partons, m_T^2, given by,

$$\mu^2 = m_T^2 = \tfrac{1}{2}(m_1^2 + p_{T1}^2 + m_2^2 + p_{T2}^2)$$

The parton shower is conceptually the same in both generators. However, in PYTHIA, the evolution is ordered in the virtuality of the radiated partons. The partons are hadronised using the Lund Symmetric String Fragmentation model [22]. In the Lund Model, partons are connected via strings, the strength of which is $\sim$ 1GeVfm^{-1}. As the partons move away from each other, the strings become more energetic and finally break to produce $q\bar{q}$ pairs. When the energy of a string is too small to enable further separation of the partons, hadrons are formed. Finally, the unstable hadrons are decayed as in HERWIG.

D.2.1 Implementation of Multiparton Interactions in PYTHIA

The model for multiparton interactions in PYTHIA is based on the assumption that the partonic interactions in an event form a decreasing series in $\hat{p}_T$ [23]. Whilst HERWIG makes a prediction for the total non-diffractive photon-proton cross-section, $\sigma_{ND}^{\gamma p}$, PYTHIA uses measured values. The probability that in a given photon-proton interaction, a hard interaction with $\hat{p}_T$ takes place is,

$$P(\hat{p}_T^2) = \frac{1}{\sigma_{ND}^{\gamma p}} \frac{d\sigma_{QCD}^{\gamma p}}{d\hat{p}_T^2}(\hat{p}_T^2) \tag{D8}$$

In the decreasing series in $\hat{p}_T$, the probability that the hardest scatter takes place at a certain $\hat{p}_{T1}$ is then,

$$P(\hat{p}_{T1}^2)\exp\left(-\int_{\hat{p}_{T1}^2}^{W^2/4} P(\tilde{p}_T^2)d\tilde{p}_T^2\right) \tag{D9}$$

This is the product of the probability that a scatter takes place at this $\hat{p}_{T1}^2$ (from (D8)), and the probability that between a maximum value $\sqrt{W^2/4}$ and $\hat{p}_{T1}$, no further scatter occurs. Following this logic, the probability for the n^{th} scatter at $\hat{p}_{Tn}$ is,

$$P(\hat{p}_{Tn}^2)\frac{1}{(n-1)!}\left(\int_{\hat{p}_{Tn}^2}^{W^2/4} P(\tilde{p}_T^2)d\tilde{p}_T^2\right)^{n-1} \exp\left(-\int_{\hat{p}_{Tn}^2}^{W^2/4} P(\tilde{p}_T^2)d\tilde{p}_T^2\right) \tag{D10}$$

Taking the sum over n is equivalent to not asking which scatter in the series takes place at this $\hat{p}_T$ and, as should be the case, the result is the original probability of equation (D8),

$$\Sigma_{n=1}^{\infty} P(\hat{p}_{Tn}^2)\frac{1}{(n-1)!}\left(\int_{\hat{p}_{Tn}^2}^{W^2/4} P(\tilde{p}_T^2)d\tilde{p}_T^2\right)^{n-1} \exp\left(-\int_{\hat{p}_{Tn}^2}^{W^2/4} P(\tilde{p}_T^2)d\tilde{p}_T^2\right) = P(\hat{p}_T^2) \tag{D11}$$

This also shows that, on average, this method of finding the probability for the n^{th} scatter gives the correct number of scatters per photon-proton interaction,

$$\int_{\hat{p}_{Tmin}^2}^{W^2/4} P(\hat{p}_T^2)d\hat{p}_T^2 = \frac{1}{\sigma_{ND}^{\gamma p}} \int_{\hat{p}_{Tmin}^2}^{W^2/4} \frac{d\sigma_{QCD}^{\gamma p}}{d\hat{p}_T^2} d\hat{p}_T^2 = \frac{\sigma_{QCD}^{\gamma p}(\hat{p}_{Tmin}^2)}{\sigma_{ND}^{\gamma p}} \tag{D12}$$

For each event, starting from a maximum value $\sqrt{W^2/4}$, the partonic interactions are generated according to the probabilities from (D9). For the additional scatters, the parton distribution functions must depend on all the preceding x values and flavours chosen. However, not enough is known about hadrons to write down such correlated probability distributions. To take account of the energy that has already gone into the previous scatters, PYTHIA uses $x = \frac{x_n}{\Sigma_{i=1}^{n-1} x_i}$ instead of x_n, to evaluate the parton distribution functions for the n^{th} scatter.

PYTHIA, like HERWIG, produces all additional interactions as $gg \to gg$, where the two outgoing gluons form a colour singlet. In this way, they are decoupled from the rest of the event and the problem of connecting the colour lines from different scatters is avoided.

The number of interactions per event has a Poisson distribution about the average, $\langle n \rangle$. Therefore, according to this model, there is a probability $\exp(-\langle n \rangle)$ that events without a hard partonic interaction, but in which there is a soft interaction, must be generated. However, in the Monte Carlo samples used for this analysis, every event was required to have a hard subprocess with $\hat{p}_T > \hat{p}_T^{min}$. Unlike HERWIG, the $\hat{p}_T^{min}$ threshold for the additional scatters can be set separately in PYTHIA.

References

[1] ZEUS Collaboration, M. Derrick et al., Phys. Lett. **B322** (1994) 287

[2] ZEUS Collaboration; J.Breitweg et al., "Measurement of Three-Jet Distributions in Photoproduction at HERA", DESY 98-162 (1998)

[3] B. R. Martin, G. Shaw, "Particle Physics", Wiley (1992)

[4] ZEUS Collaboration, M. Derrick et al., Phys. Lett. **B316** (1993) 412
H1 Collaboration, I. Abt et al, Nucl. Phys. **B407** (1993) 515
ZEUS Collaboration, M. Derrick et al, Z. Phys. **C65** (1995) 379

[5] ZEUS Collaboration, M. Derrick et al., Phys. Letter **B293** (1992) 465

[6] ZEUS Collaboration, M. Derrick et al., The ZEUS Detector Status report 1993, DESY 1993

[7] F. Jacquet and A. Blondel, in "Proceedings of the study for an *ep* Facility for Europe", ed. U. Amaldi (DESY 79/48 1979) 391

[8] S. Catani, Yu. L. Dokshitzer, B. R. Webber, Phys. Lett. **B285** (1992) 291

[9] S. Catani, Yu. L. Dokshitzer, M. H. Seymour, B. R. Webber, Nucl. Phys, **B406** (1993) 187

[10] S. D. Ellis, D. E. Soper, Phys. Rev. **D48** (1993) 3160

[11] P. J. Bussey, EUCELL, ZEUS PHANTOM Users Library

[12] P. de Jong "Status of the Uranium Calorimeter Reconstruction Software", Zeus Note 92-019

[13] H. Abramowicz, A. Caldwell, R. Sinkus "Neural Network Based Electron Identification in the ZEUS Calorimeter", DESY 95-054
R.Sinkus, Nucl. Instum. Methods **A361** (1995) 290

[14] HERWIG 5.9; G. Marchesini, B. R. Webber, G. Abbiendi, I. G. Knowles, M. H. Seymour, L. Stanco, Computer Phys. Commun. 67 (1992) 465

[15] PYTHIA 5.7; T. Sjöstrand, Computer Phys. Commun. 82 (1994) 74

[16] M. Glück, E. Reya, A. Vogt, Phys. Rev. **D46** (1992) 1973
M. Glück, E. Reya, A. Vogt, Phys. Rev. **D45** (1992) 3986

[17] K. Hagiwara et al., Phys. Rev. **D51** (1995) 3197

[18] T. Asakawa and S. Geer, Phys. Rev. **D53**, 4793 (1996)

[19] S. Bentvelsen, J. Engelen, P. Kooijman in "Physics at HERA", Vol.1, edited by W. Buchmüller, G. Ingelman (Proceedings of the Workshop, Hamburg, 1991), p23

[20] J. Huth et al., Proceedings of the 1990 DPF Summer Study on High Energy Physics, Snowmass, Colorado, edited by E. L. Berger World Scientific, Singapore (1992) p134

[21] JADE Collaboration, Phys. Lett. **B213-235** (1988)

[22] B. Andersson, G. Gustafson, G. Ingelman, T. Sjöstrand, Phys. Rep. 97 (1983) 33

[23] J. M. Butterworth, J. R. Forshaw, M. H. Seymour, "Multiparton Interactions in Photoproduction at HERA", CERN-TH/95-82

[24] J. M. Butterworth, J. R. Forshaw, DESY 93-107 (1993)

[25] QCD and Collider Physics, R. K. Ellis, W. J. Stirling, B. R. Webber, Cambridge University Press

[26] R. L. Saunders, Ph.D Thesis, University College London (1997)

[27] L. E. Sinclair, Ph.D Thesis, McGill University, Montreal (1995)

[28] M. R. Sutton, Ph.D Thesis, University College London (1998)

[29] M. Wing, Ph.D Thesis, University College London (1999)

[30] M. H. Seymour, "Introduction to QCD", Oxford Lecture Notes, Hilary Term (2000)